Available online at www.sciencedirect.com
ScienceDirect
Journal of Magnetic Resonance 187 (2007) 66–77
JMR Journal of Magnetic Resonance
www.elsevier.com/locate/jmr

Targeted-ROI imaging in electron paramagnetic resonance imaging

Xiaochuan Pan [a,c], Dan Xia [a], Howard Halpern [b,c,*]

[a] Department of Radiology, The University of Chicago, Chicago, IL 60637-7117, USA
[b] Department of Radiation and Cellular Oncology, The University of Chicago, MC 1105, Chicago, IL 60637-7117, USA
[c] Center for EPR Imaging In Vivo Physiology, The University of Chicago, MC 1105, Chicago, IL 60637-7117, USA

Received 8 April 2006; revised 17 February 2007
Available online 23 February 2007

Abstract

Electron paramagnetic resonance imaging (EPRI) is a technique that has been used for *in vivo* oxygen imaging of small animals. In continuous wave (CW) EPRI, the measurement can be interpreted as a sampled 4D Radon transform of the image function. The conventional filtered-backprojection (FBP) algorithm has been used widely for reconstructing images from full knowledge of the Radon transform acquired in CW EPRI. In practical applications of CW EPRI, one often is interested in information only in a region of interest (ROI) within the imaged subject. It is desirable to accurately reconstruct an ROI image only from partial knowledge of the Radon transform because acquisition of the partial data set can lead to considerable reduction of imaging time. The conventional FBP algorithm cannot, however, reconstruct accurate ROI images from partial knowledge of the Radon transform of even dimension. In this work, we describe two new algorithms, which are referred to as the backprojection filtration (BPF) and minimum-data filtered-backprojection (MDFBP) algorithms, for accurate ROI-image reconstruction from a partial Radon transform (or, truncated Radon transform) in CW EPRI. We have also performed numerical studies in the context of ROI-image reconstruction of a synthetic 2D image with density similar to that found in a small animal EPRI. This demonstrates both the inadequacy of the conventional FBP algorithm and the success of BPF and MDFBP algorithms in ROI reconstruction. The proposed ROI imaging approach promises a means to substantially reduce image acquisition time in CW EPRI.

Keywords: EPR imaging; Filtered-backprojection; Backprojection-filtration; Spectral-spatial EPR imaging; Spectroscopic EPR imaging; Image theory

1. Introduction

Electron paramagnetic resonance imaging (EPRI) is an emerging technique for *in vivo* imaging of the spatial and spectral distribution of the absorption and dispersion of radio-frequency (RF) energy by an extended sample of paramagnetic probes in a living subject [1–3]. Images of water soluble radical probes that have been administered into living animals provide physiologic information of interest with a high sensitivity. Using radical probes that are designed to be sensitive to specific aspects of physiology, measurable, and imageable quantities include the distribution of endogenous or introduced paramagnetic species, tissue redox status, pH value, and microviscosity. One particularly important aspect that has received significant attention is the imaging of tissue oxygen concentration within tumors [4,5].

It is difficult to generate pulsed gradients of any substantial magnitude for subjects larger than a few millimeters because of the extremely short time of electron-spin relaxation in the majority of the species of interest. Therefore, EPRI systems often employ continuous wave (CW) spectrometers in combination with fixed stepped field gradients for data acquisition [6–9]. It has been shown [10,11] that the measurable data function in CW EPRI can be interpreted as the Radon transform of the object function, which is the spectral-spatial distribution of the electron spins of the radical probe. Therefore, the task of spatial-

* Corresponding author. Fax: +1 773 702 5940.
E-mail address: h-halpern@uchicago.edu (H. Halpern).

1090-7807/$ - see front matter © 2007 Elsevier Inc. All rights reserved.
doi:10.1016/j.jmr.2007.02.010

spectral image reconstruction in CW EPRI is tantamount to the task of image reconstruction from the Radon transform of the object function. One can extract parameters of interest, such as the spectrum width, at each spatial point [12,13], and thus these extracted parameters form parameter images such as oxygen concentration images that are of potential clinical value.

In EPRI, one is often interested in information only about a region of interest (ROI) within the subject, such as an ROI containing a tumor. Current algorithms for CW EPRI require full knowledge of the Radon transform of the object function for accurate reconstruction of an ROI image. However, a long data-acquisition time is generally required for measuring full knowledge of the Radon transform, thus significantly limiting the capability of performing *in vivo* and/or temporally longitudinal EPRI studies. If one can accurately reconstruct ROI images from incomplete knowledge of the Radon transform, one needs only to collect a portion of the Radon transform, thus reducing the imaging time. Photon based tomography, e.g., computed tomography (CT), positron emission tomography (PET), or single-photon emission computed tomography (SPECT) are generally constructed with fixed numbers of receiver elements defining a fixed number of projection samples. CW EPRI is much more flexible in that projection sampling can be adjusted to vary both the number of samples in a projection and the field interval of the projection through a simple set of commands to a D/A converter in a current controlled power supply. Thus, projection truncation is readily achieved and can be translated into a reduction in acquisition time. In this work, we study ROI-image reconstruction from the truncated Radon transform of an object function. The work reported here is of theoretical value because it reveals that, in CW EPRI, ROI images can accurately be reconstructed from a truncated, even-dimensional Radon transform [14,15]. It also has practical implications for rapid CW EPRI because acquisition of only partial knowledge of the Radon transform can substantially reduce imaging time.

In Section 2, we briefly review the data function and conventional image reconstruction in CW EPRI. In Section 3 we introduce the chord-based image reconstruction, a new approach to image reconstruction from the Radon transform. In Section 4, we develop two algorithms capable of reconstructing accurate ROI images from a truncated Radon transform. In Section 5, we perform numerical studies to quantitatively demonstrate and validate the proposed algorithms. Finally, conclusions and remarks are made in Section 6.

2. EPR Imaging

In CW EPRI of n-dimensions (nD), the object function $f(\vec{r})$ includes $n-1$ spatial dimensions and one spectral dimension. We assume that $f(\vec{r})$ has a compact support Ω in the nD space, i.e., $f(\vec{r}) = 0$ if vector $\vec{r} \notin \Omega$. This is guaranteed by the spatial limitation of the distribution of RF field greater than some infinitesimal value and the spatial limitation of the receiver to detect a signal smaller than that infinitesimal value. From the spectral dimension of the support of the object function $f(\vec{r})$ one can readily estimate parameters, such as the spectral width of the radical probes, that are of physiologic significance. It has been shown [16,11] that the Radon transform of $f(\vec{r})$ can be obtained from knowledge of the measurements in CW EPRI. Therefore, image reconstruction in CW EPRI is equivalent to image reconstruction from its Radon transform. Throughout this paper, we assume that the Radon transform of the object function can be estimated from the EPRI measurements.

2.1. Data function in CW EPRI

Let $p(u, \hat{e}_u)$ denote the Radon transform of the object function $f(\vec{r})$, which can be written as

$$p(u, \hat{e}_u) = \int_{\mathbb{R}^n} d\vec{r} f(\vec{r}) \delta(u - \vec{r} \cdot \hat{e}_u). \tag{1}$$

In CW EPRI, $2 \leqslant n \leqslant 4$. The unit vector $\hat{e}_u$ on a *hemi-unit* sphere $\mathbb{S}^{n-1}$ of nD indicates the direction of the hyperplane over which the integral in Eq. (1) is defined, and $u \in \mathbb{R}$ indicates the distance of the hyperplane from the origin.

2.2. Conventional image reconstruction in CW EPRI

Images can be reconstructed from the Radon transform by use of the conventional filtered-backprojection (FBP) algorithm [17,18], which can be written as

$$f(\vec{r}) = \int_{\mathbb{S}^{n-1}} d\hat{e}_u \int_{\mathbb{R}} dv_u |v_u|^{n-1} P(v_u, \hat{e}_u) e^{2\pi j v_u u} \Big|_{u=\vec{r}\cdot\hat{e}_u}, \tag{2}$$

where $\vec{r} \in \mathbb{R}^n$, and $P(v_u, \hat{e}_u)$ is the 1D Fourier transform of $p(u, \hat{e}_u)$ with respect to u.

The conventional FBP algorithms for odd and even dimensional Radon transforms differ fundamentally from each other [17,18]. For the odd dimensional Radon transform, the filter $|v_u|^{n-1}$ becomes v_u^{n-1}, which is equivalent to taking the $(n-1)th$-order derivative of $p(u, \hat{e}_u)$ with respect to u. Consequently, the conventional FBP algorithm invokes only local operations, thus allowing accurate ROI-image reconstruction from truncated Radon transforms of odd dimensions. On the other hand, for the even dimensional Radon transform, $|v_u|^{n-1}$ becomes $\mathrm{sgn}[v_u] v_u^{n-1}$, which is equivalent to taking a Hilbert transform of the $(n-1)th$-order derivative of $p(u, \hat{e}_u)$. Because the Hilbert transform represents a non-local operation, the conventional FBP algorithm cannot accurately reconstruct images from the truncated Radon transform of even dimension.

As discussed above, one is often interested only in knowledge of an ROI image in CW EPRI. For a CW EPRI of even-dimensions, it is of practical significance to reconstruct accurate ROI images from limited knowledge of the Radon transform, or, equivalently, from the Radon

transform containing truncations. As we show below, this can be achieved through image reconstruction on chords.

3. New approach to image reconstruction in CW EPRI

In this section, we introduce the concept of chords and a formula for image reconstruction on chords from the Radon transform. Based upon this formula, two algorithms can be derived for accurate ROI-image reconstruction from the truncated Radon transform.

3.1. Chords in image space

In the last few years, significant advances have been made in algorithm development for image reconstruction on chords from the X-ray transform, an integral of the object function over a line [19–21]. Recently, we have also developed a theory for image reconstruction on chords from the nD Radon transform, which, when $n > 2$, represents an integral of the object function over a hyperplane. One of the potential advantages of this new theory is that algorithms can be devised for accurate ROI-image reconstruction from Radon transforms containing truncations.

Let $\vec{r}_1$ and $\vec{r}_2$ denote two pre-selected points in the image space. We refer to the straight line determined by the two points as the chord [21]. The direction of the chord is defined as

$$\hat{e}_c = \frac{\vec{r}_2 - \vec{r}_1}{|\vec{r}_2 - \vec{r}_1|}. \tag{3}$$

Let $x_c \in \mathbb{R}$ denote the coordinate along the chord, a signed distance from the chord center. Therefore, a given point $\vec{r}$ on the chord can be expressed as

$$\vec{r} = \frac{1}{2}(\vec{r}_1 + \vec{r}_2) + x_c \hat{e}_c. \tag{4}$$

We show in Fig. 1 how chords are defined in the image space. Depending upon the selected points, the directions of chords can be different.

3.2. Division of the backprojection directions

As it can be observed in Eq. (2), each of the unit vectors $\hat{e}_u$ on the hemi-unit sphere $\mathbb{S}^{n-1}$ specifies the backprojection direction. For a given chord on which the image is to be reconstructed, the set of backprojection unit vectors $\hat{e}_u$ on $\mathbb{S}^{n-1}$ can be divided into two subsets: $\mathbb{S}_+^{n-1}$ and $\mathbb{S}_-^{n-1}$.

The unit vectors $\hat{e}_u$ on $\mathbb{S}_+^{n-1}$ satisfy

$$\operatorname{sgn}[\hat{e}_c \cdot \hat{e}_u] = 1, \tag{5}$$

where sgn denotes the sign function, whereas the unit vectors $\hat{e}_u$ on $\mathbb{S}_-^{n-1}$ satisfy

$$\operatorname{sgn}[\hat{e}_c \cdot \hat{e}_u] = -1. \tag{6}$$

In Fig. 2, we display, for a given chord (i.e., a given $\hat{e}_c$), how the backprojection directions (i.e., the set of $\hat{e}_u$) are separated, according to Eqs. (5) and (6), into two groups.

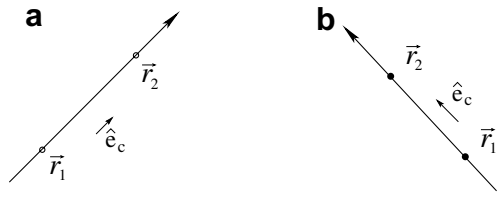

Fig. 1. (a) A chord specified by a pair of pre-selected points in the image space. (b) A chord determined by another pair of pre-selected points in the image space. It should be noted that the two chords have different directions.

3.3. Reconstruction of images on chords

It can be observed that the image space can completely be covered with chords. Therefore, the task of image reconstruction can be accomplished through reconstructing images on the chords that fill the image space. Moreover, a given ROI within the image support can be filled completely by a set of chords intersecting the ROI. Therefore, image reconstruction within an ROI is tantamount to that on the chords intersecting the ROI. In Fig. 3, we show how the 2D image space and the corresponding ROI can be covered by chords with different unit vectors $\hat{e}_c$.

As discussed in Section 2.2 above, it is well-known that an accurate ROI image can be reconstructed from the Radon transform of odd dimension containing truncation. Recently, it was demonstrated that it is possible to reconstruct an accurate ROI image from the Radon transform of even dimension containing truncations [22]. We describe below a general formula for image reconstruction on a chord from the Radon transform of even dimension.

Consider a point $\vec{r}$ on a chord along the direction $\hat{e}_c$. Starting from the conventional FBP algorithm in Eq. (2), one can show [22] that, for a point $\vec{r}$ on the chord, the object function is given by

$$f(\vec{r}) = \int_{\mathbb{R}^n} d\vec{r}' K(\vec{r}, \vec{r}') g(\vec{r}'), \tag{7}$$

where the kernel $K(\vec{r}, \vec{r}')$ is given by

$$K(\vec{r}, \vec{r}') = \frac{2}{(2\pi j)^{n-1}} \int_{\mathbb{R}^n} d\vec{v} (\operatorname{sgn}[\vec{v} \cdot \hat{e}_c])^{n-1} e^{2\pi j \vec{v} \cdot (\vec{r} - \vec{r}')}, \tag{8}$$

and the backprojection image $g(\vec{r}')$ can be expressed as

$$g(\vec{r}') = \int_{\mathbb{S}_+^{n-1}} d\hat{e}_u \left[\frac{\partial^{n-1}}{\partial u^{n-1}} p(u, \hat{e}_u) \right]_{u = \vec{r}' \cdot \hat{e}_u} + (-1)^{n-1} \times \int_{\mathbb{S}_-^{n-1}} d\hat{e}_u \left[\frac{\partial^{n-1}}{\partial u^{n-1}} p(u, \hat{e}_u) \right]_{u = \vec{r}' \cdot \hat{e}_u}, \tag{9}$$

with $\vec{r}' \in \mathbb{R}^n$. The formula specified by Eqs. (7)–(9) provides the basis for algorithm development for image reconstruction on a chord from the Radon transform. We point out again that only the Radon transform of even dimension will be considered here because reconstruction from a truncated Radon transform of odd dimension is well-known.

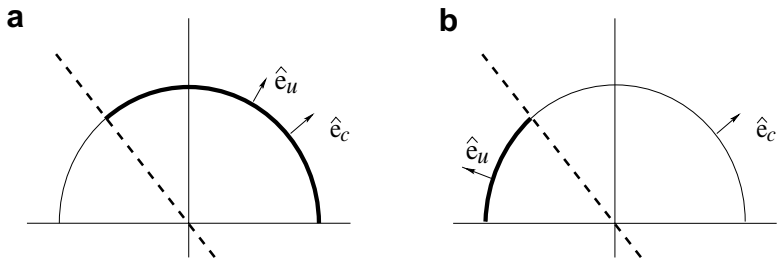

Fig. 2. For a given chord direction $\hat{e}_c$, the backprojection directions $\hat{e}_u$ on the hemi-unit sphere $\mathbb{S}^{n-1}$ are divided into two groups. (a) The inner products between $\hat{e}_c$ and $\hat{e}_u$ in this group are positive, whereas (b) the inner products between $\hat{e}_c$ and $\hat{e}_u$ in this group are negative.

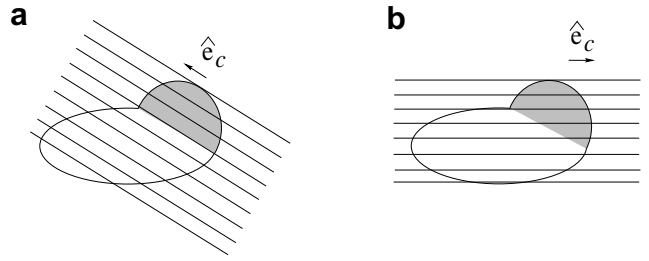

Fig. 3. (a) The image space and an ROI (shaded region) can be filled completely by a set of parallel chords. (b) The image space and an ROI (shaded region) can also be filled completely by a different set of parallel chords.

4. New algorithms for ROI-image reconstruction in CW EPRI

We use $f_c(x_c,\vec{r}_1,\vec{r}_2)$ and $g_c(x_c,\vec{r}_1,\vec{r}_2)$ to denote the object function and backprojection image at point $x_c \in \mathbb{R}$ on the chord specified by $\vec{r}_1$ and $\vec{r}_2$. Therefore, we have

$$\begin{aligned} f(\vec{r}) &= f_c(x_c,\vec{r}_1,\vec{r}_2) \\ g(\vec{r}) &= g_c(x_c,\vec{r}_1,\vec{r}_2), \end{aligned} \tag{10}$$

where $\vec{r}$ and x_c are related through Eq. (4). It should be pointed out that the functional forms of $f(\vec{r})$ and $g(\vec{r})$ generally differ from that of $f_c(x_c,\vec{r}_1,\vec{r}_2)$ and $g_c(x_c,\vec{r}_1,\vec{r}_2)$.

Because the object function is assumed to have a compact support Ω, the intersection of a chord with Ω, which we refer to as the *support segment* on the chord, is always finite, as shown in Fig. 4a. This important observation will be exploited below for deriving algorithms for image reconstruction on the support segment from knowledge of the backprojection image only on the support segment, as shown in Fig. 4b. Furthermore, because the calculation of the backprojection image on the support segment requires knowledge of the Radon transform derivatives only on the projections of the support segment, the final image on the support segment can accurately be reconstructed from knowledge of the Radon transform derivative only from the projections of the support segment.

4.1. The backprojection-filtration (BPF) algorithm

We use x_{s1} and x_{s2} to denote the endpoints of the support segment on a chord, where $x_{s1} \leqslant x_{s2}$. Therefore, $f_c(x_c,\vec{r}_1,\vec{r}_2) = 0$ for $x_c \in (-\infty,x_{s1}]$ and for $x_c \in [x_{s2},\infty)$. Consider two parameters x_{c1} and x_{c2} that satisfy $x_{c1} \in (-\infty,x_{s1}]$ and $x_{c2} \in [x_{s2},\infty)$. It has been shown [22] that the image on the support segment of the chord is given by

$$f_c(x_c,\vec{r}_1,\vec{r}_2) = \frac{2}{(j2\pi)^n}\sqrt{\frac{(x_c-x_{c2})}{(x_c-x_{c1})}}\int_{\mathbb{R}}\frac{dx'_c}{x'_c-x_c}g_{\Pi}(x'_c,\vec{r}_1,\vec{r}_2), \tag{11}$$

where

$$g_{\Pi}(x'_c,\vec{r}_1,\vec{r}_2) = \Pi_c(x'_c)\sqrt{\frac{(x'_c-x_{c1})}{(x'_c-x_{c2})}}g_c(x'_c,\vec{r}_1,\vec{r}_2), \tag{12}$$

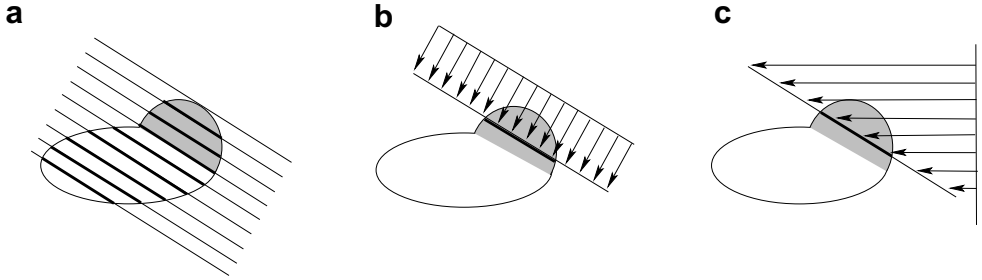

Fig. 4. (a) The support segment (thick segment) is defined as the portion of the chord within the support of the object function. (b) and (c) Backprojections of the Radon transform onto the chord at two different views. Algorithms derived here can reconstruct accurately an image on the support segment from knowledge of the backprojection only on the support segment.

and $\Pi_c(x'_c) = 1$ for $x'_c \in [x_{c1}, x_{c2}]$ and $\Pi_c(x'_c) = 0$ for $x'_c \notin [x_{c1}, x_{c2}]$. We refer to the algorithm described in Eq. (11) as the backprojection-filtration (BPF) algorithm because it backprojects the Radon transform derivatives (i.e., the integration over $\hat{e}_u$ for obtaining $g_c(x'_c, \vec{r}_1, \vec{r}_2)$) before performing the 1D Hilbert transform of the weighted backprojection (i.e., the integration over x'_c). Thus, only the interval $[x_{c1},x_{c2}]$ contributes to the integral in Eq. (11).

4.2. The minimum-data filtered-backprojection (MDFBP) algorithm

The BPF algorithm described above reconstructs the image on a chord by performing a 1D Hilbert transform of the backprojection image on the chord. On the other hand, it is also possible to reconstruct the image on a chord by performing the 1D Hilbert transform of the Radon transform derivative prior to its backprojection onto the chord. We have also derived such an algorithm, which has been referred to as the minimum-data filtered backprojection (MDFBP) algorithm [23]. Let u_c denote the projection of a point $\vec{r}$ on the chord along $\hat{e}_u$. It can be written as

$$u_c = \vec{r} \cdot \hat{e}_u = \frac{1}{2}(\vec{r}_1 + \vec{r}_2) \cdot \hat{e}_u + x_c \hat{e}_c \cdot \hat{e}_u. \tag{13}$$

Using x_{c1} and x_{c2} to replace x_c in Eq. (13), we obtain the projections u_{c1} and u_{c2} of the two points, x_{c1} and x_{c2}, on the chord. The MDFBP algorithm can be written as

$$\begin{aligned} f_c(x_c, \vec{r}_1, \vec{r}_2) = \frac{2}{(j2\pi)^n} \sqrt{\frac{(x_c - x_{c2})}{(x_c - x_{c1})}} \Bigg[& \int_{\mathbb{S}_+^{n-1}} d\hat{e}_u \\ & \times \int_{\mathbb{R}} \frac{du'_c}{u'_c - u_c} \sqrt{\frac{(u'_c - u_{c1})}{(u'_c - u_{c2})}} \bar{p}(u'_c, \hat{e}_u) \\ & - \int_{\mathbb{S}_-^{n-1}} d\hat{e}_u \int_{\mathbb{R}} \frac{du'_c}{u'_c - u_c} \\ & \times \sqrt{\frac{(u'_c - u_{c1})}{(u'_c - u_{c2})}} \bar{p}(u'_c, \hat{e}_u) \Bigg], \end{aligned} \tag{14}$$

where u'_c is obtained by use of x'_c to replace x_c in Eq. (13),

$$\bar{p}(u'_c, \hat{e}_u) = \Pi_c(u'_c) \frac{\partial^{n-1}}{\partial u^{n-1}} p(u, \hat{e}_u) \Big|_{u=u'_c}, \tag{15}$$

and $\Pi_c(u'_c) = 1$ for $u'_c \in [u_{c1}, u_{c2}]$ and $\Pi_c(u'_c) = 0$ for $u'_c \notin [u_{c1}, u_{c2}]$. In fact, $[u_{c1},u_{c2}]$ is the projection of $[x_{c1},x_{c2}]$ at view $\hat{e}_u$. We refer to the algorithm described in Eq. (14) as the MDFBP algorithm because it performs the 1D Hilbert transform of the Radon transform derivative along the projection of the chord (i.e., the integration over u'_c) followed by the backprojection onto the chord (i.e., the integration over $\hat{e}_u$) and because it requires less data than does the conventional FBP algorithm. It should be pointed out that the MDFBP algorithm differs fundamentally from the conventional FBP algorithm because the latter cannot accurately reconstruct ROI images from truncated Radon transforms of even dimensions.

4.3. ROI-image reconstruction from the truncated Radon transform

As shown in Eqs. (12) and (15), the rectangular function Π_c allows the BPF and MDFBP algorithms to reconstruct images from knowledge of the Radon transform *only* on the projection (i.e., on $[u_{c1},u_{c2}]$) of the chord segment (i.e., of $[x_{c1},x_{c2}]$). Therefore, with respect to the entire support of the object function, even if the Radon transform is truncated at certain views $\hat{e}_u$, an accurate image on the chord can still be reconstructed. We now use 2D examples to illustrate how ROI images can be reconstructed accurately from the truncated Radon transform of even dimension by use of the BPF and MDFBP algorithms described above.

Consider image reconstruction on the chord shown in Fig. 5a. At the two views displayed in Figs. 5b and c, the BPF and MDFBP algorithms require knowledge of the Radon transform derivative only on $[u_{c1},u_{c2}]$, which are the projections of the support segments onto the detector lines. This interval pertains to integration over only the indicated chord. It can be seen that data are truncated at these views relative to the entire support of the object function, which is enclosed by the thin curve. In this sense, the BPF and MDFBP algorithms can accurately reconstruct the chord image from the truncated Radon transform.

In Fig. 6a, we show an ROI that is covered completely by the set of support segments. As discussed above, accurate image reconstruction on one of these support segments needs knowledge of the Radon transform only

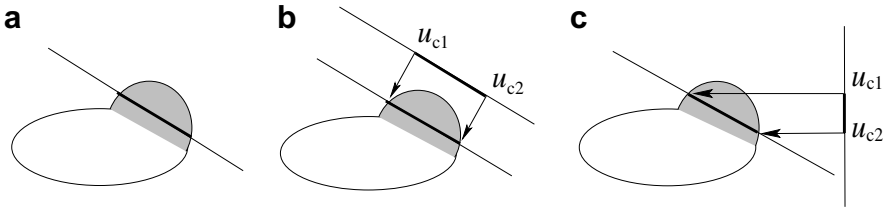

Fig. 5. (a) A chord (thin line) and its support segment (thick line segment). (b) and (c) Knowledge of the Radon transform on $[u_{c1}, u_{c2}]$ at two views necessary for image reconstruction on the chord. It can be observed that data available at the two views are truncated with respect the support of the object function.

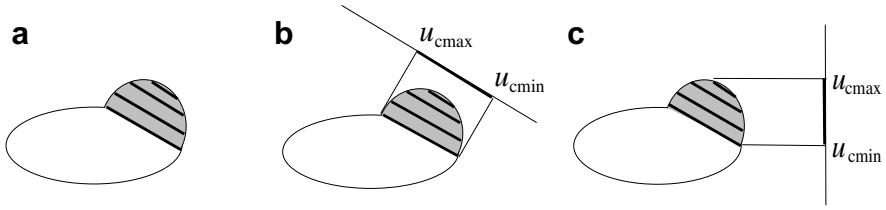

Fig. 6. (a) An ROI (shaded region) in the support of the object function. It can be filled by the support segments (thick line segments). (b) Knowledge of the Radon transform only on the union $[u_{cmin},u_{cmax}]$ of the projections of these support segments at a view $\hat{e}_u$. (c) Knowledge of the Radon transform only on the union $[u_{cmin},u_{cmax}]$ of the projections of these support segments at another view $\hat{e}_u$. Clearly, the Radon transform on these unions is truncated relative to the support of the object function.

on the projection $[u_{c1},u_{c2}]$ of that support segment, as shown in Figs. 5b and c. Therefore, image reconstruction within the ROI (or, equivalently, image reconstruction on all of the support segments covering the ROI) needs knowledge of the Radon transform only on the union $[u_{cmin},u_{cmax}]$ of these projections $[u_{c1},u_{c2}]$ of the support segments. In other words, the BPF and MDFBP algorithms can accurately reconstruct ROI images by reconstructing images on support segments covering the ROI from the truncated Radon transform. The discussion above for ROI-image reconstruction from the truncated 2D Radon transform is directly applicable to ROI-image reconstruction from truncated nD, including 4D, Radon transforms.

4.4. Implementation of the BPF and MDFBP algorithms

4.4.1. Implementation of the BPF algorithm

(a) Determining a set of chords that completely cover the image support of the ROI. One can often select a set of chords that are parallel to one of the axes of the laboratory coordinate system.
(b) Computing the backprojection image, according to Eq. (9), onto a chord in the set for $x'_c \in [x_{c1}, x_{c2}]$ and then calculating the weighted backprojection image on the chord according to Eq. (12).
(c) Performing the Hilbert transform of the weighted backprojection image and multiplying the factor to yield the final image according to Eq. (11). The Hilbert transform can readily be calculated through the use of the fast Fourier transform (FFT) technique.
(d) Repeating steps (b) and (c) for all of the chords in the set to yield the final ROI image. These steps can be done on the whole object function taken as the ROI as shown below.

4.4.2. Implementation of the MDFBP algorithm

(a) Determining a set of chords that completely cover the image support of the ROI. One can often select a set of chords that are parallel to one of the axes of the laboratory coordinate system.
(b) Computing data derivatives according to Eq. (15).
(c) Performing the Hilbert transform of the weighted data derivatives (i.e., the integration over u'_c) in Eq. (14). Again, the Hilbert transform can readily be calculated through the use of the FFT technique.
(d) Backprojecting the filtered data onto the chord for $x'_c \in [x_{c1}, x_{c2}]$ and multiplying the weighting factor in Eq. (14) to yield the final image on the chord.
(e) Repeating steps (b)–(d) for all of the chords in the set to yield the final full or ROI images.

5. Numerical results

We have performed numerical studies to validate the proposed algorithms and to demonstrate ROI-image reconstruction in 2D CW EPRI. In Section 5.2, we reconstruct 2D spatial ROI images from truncated data without considering the spectral dimension, whereas, in Section 5.4, we reconstruct 2D spectral-spatial ROI images from truncated data. Numerical investigation of ROI-image reconstruction in 4D EPRI is beyond the scope of this work and will be reported elsewhere in the future.

5.1. Spatial images and truncation data

We have created a numerical phantom, shown in Fig. 7a, to simulate a mouse that is used in our animal imaging. The structure in one of the legs of the numerical mouse phantom mimics a tumor in the leg, which is shown in Fig. 7b. We are interested in information about the tumor in the mouse leg, i.e., in the ROI enclosed by white, thick curve. as depicted in Figs. 7b and c.

Using the mouse phantom, we have generated the complete, numerical Radon transform, as displayed in Fig. 8a, which consists of 512 projection views over $[0, \pi]$. The projection data at each view contains 256 samples. In Fig. 8b, we show the truncated Radon transform that is sufficient for accurate reconstruction of the ROI image displayed in Fig. 7b. In the proposed ROI-image reconstruction, although one does not have precise knowledge of the size and shape of the part of the object to be imaged, one can always design an ROI of regular shape so that the part of the object to be imaged is completely encompassed by the designed ROI. For the ROI with a regular shape, one can readily determine the Radon subspace into which the

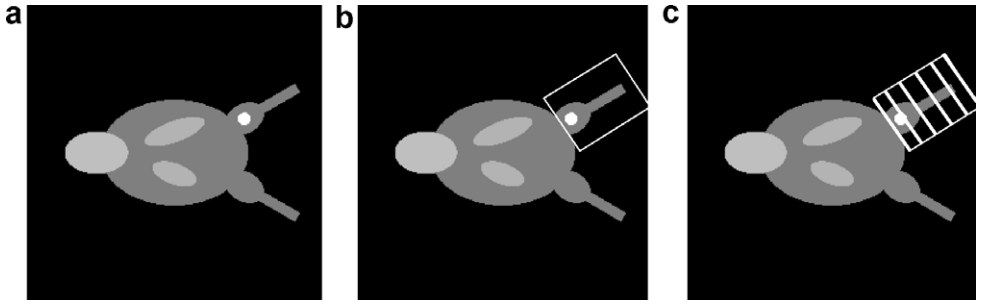

Fig. 7. (a) A numerical phantom that simulates a mouse. (b) An ROI is enclosed by the thick white curve. The ROI image containing the mouse leg and the tumor. (c) The support segments (thick line segments) of the chord that cover completely the ROI. The display window is [0.0, 2.0].

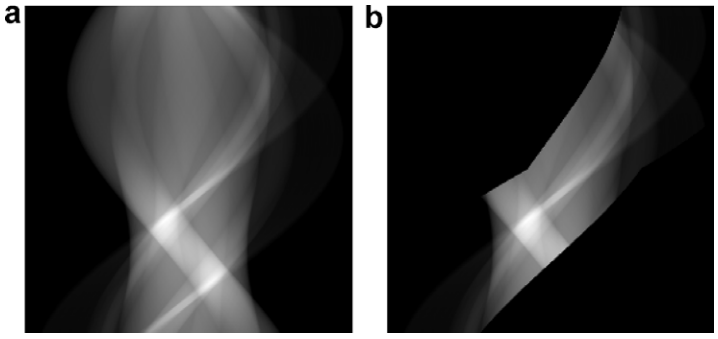

Fig. 8. (a) The full Radon transform of the mouse phantom in Fig. 7. The vertical and horizontal axes indicate the projection direction and u, respectively. (b) The phantom portion of the Radon transform required by the BPF and MDFBP algorithms for accurate image reconstruction within the indicated ROI. Clearly, this Radon transform is truncated at most of the projection views.

ROI is projected. If the support segments are enclosed by the ROI, data within this Radon subspace would be sufficient for accurately reconstructing the ROI image. The size and location of the ROI with a regular shape can be determined based upon prior information about the part of the object to be imaged, which can be obtained, e.g., through visualization of or from an initial low-resolution image of the object. It should also be noted that the size of the Radon subspace relies upon the size, shape, and location of the selected ROI. If one has precise information about the shape and size of the part of the object to be imaged, one can further reduce the Radon subspace by designing the ROI that matches the imaged part of the object. In this work, our intension is to demonstrate the ROI-image reconstruction from partial knowledge of the Radon transform. How to obtain precise information about the shape and size of the imaged part in an object for use in the design of the tightest ROI is certainly beyond the scope of the work. Because the support of the sinogram is proportional to the image acquisition time in CW EPRI, for the 2D example under study, acquisition time can be reduced by a factor of two using ROI imaging. In an attempt to generate noisy data, we added uncorrelated Gaussion noise to the noiseless data in Fig. 8. To simulate data-noise level in a typical EPRI experiment, we use a Gaussian noise with a standard deviation, which is about about 3% of the maximum value of the Radon transform in Fig. 8a.

5.2. Reconstruction of 2D spatial ROI images

We have used the conventional FBP algorithm and the BPF and MDFBP algorithms to reconstruct images from the simulated data. In the upper row of Fig. 9, we show images reconstructed from the complete data set in Fig. 8a by use of (a) the conventional FBP algorithm, (b) the BPF algorithm, and (c) the MDFBP algorithm. In an attempt to quantitatively demonstrate the reconstruction accuracy, we also plot in the lower row of Fig. 9 the image profiles (solid curves) obtained by use of (a) the conventional FBP algorithm, (b) the BPF algorithm, and (c) the MDFBP algorithm on a horizontal image line passing through the object. For comparison, the corresponding true profile (dashed line) is also included. It can be observed from these results that the BPF and MDFPB algorithms, like the conventional FBP algorithm, can reconstruct accurate images from a full data set. Furthermore, from the full data set containing noise, we also use (a) the conventional FBP algorithm, (b) the BPF algorithm, and (c) the MDFBP algorithm to reconstruct noisy images, which are shown in Fig. 10.

From the truncated data in Fig. 8b in which the truncated projections are filled in with zeros, we reconstructed ROI images by use of (a) the conventional FBP algorithm, (b) the BPF algorithm, and (c) the MDFBP algorithm, which are shown in the upper row of Fig. 11. As compared to the true ROI image shown in Fig. 7b, it can be seen that

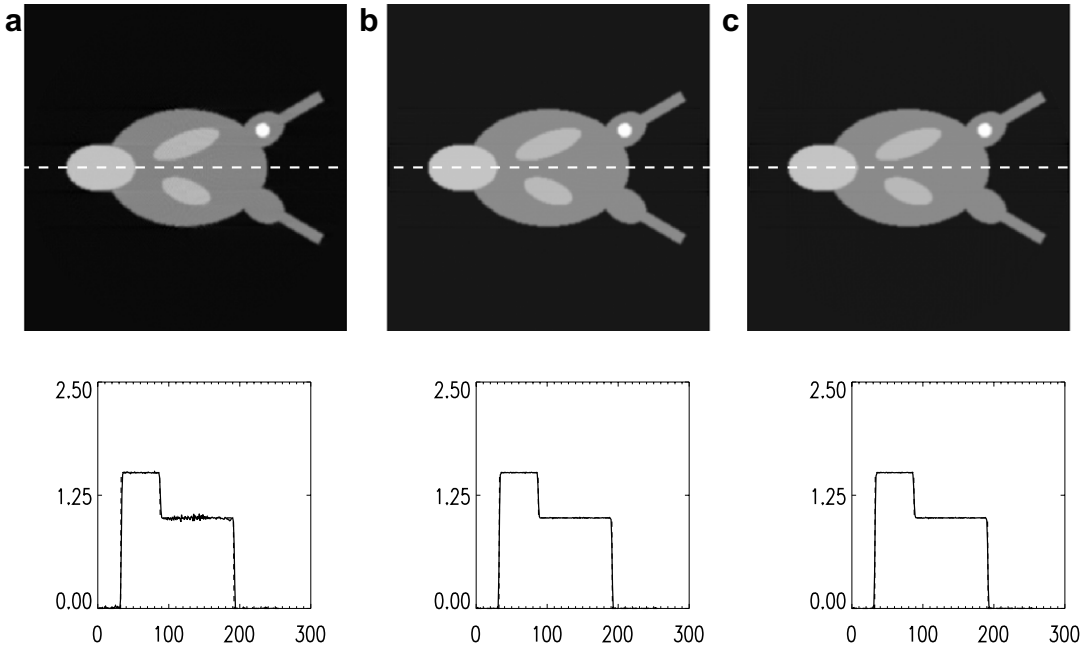

Fig. 9. Upper row: images reconstructed from the complete data set in Fig. 8a by use of (a) the conventional FBP algorithm, (b) the BPF algorithm, and (c) the MDFBP algorithm, respectively. The display window is [0.0, 2.0]. Lower row: image profiles (solid curves) obtained by use of (a) the conventional FBP algorithm, (b) the BPF algorithm, and (c) the MDFBP algorithm, respectively, on the horizontal lines passing the object in the upper row. We also display the true profile (dashed line) for comparison. It can be observed that the solid lines virtually coincide with the dashed lines, indicating that all algorithms can accurately reconstruct images from complete data.

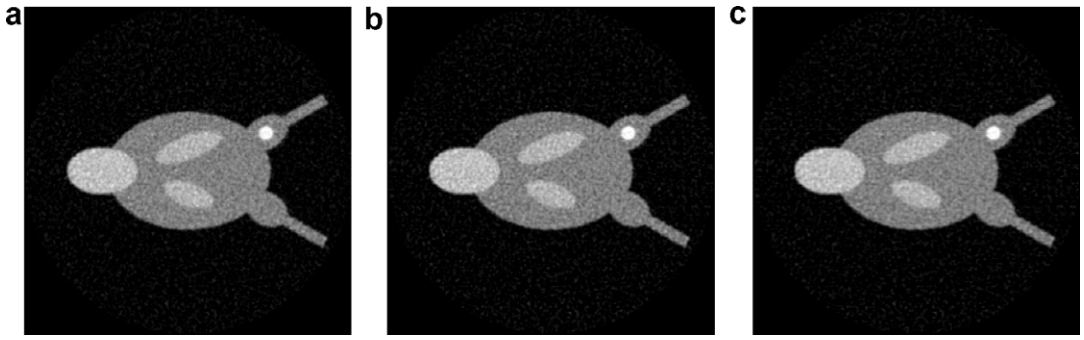

Fig. 10. Images reconstructed from the complete data set containing noise by use of (a) the conventional FBP algorithm, (b) the BPF algorithm, and (c) the MDFBP algorithm. The display window is [0.0, 2.0].

the conventional FBP algorithm cannot reconstruct accurate ROI images from truncated data, whereas the BPF and MDFBP algorithms can. We also plot in the lower row of Fig. 11 the image profiles (solid curves) obtained by use of (a) the conventional FBP algorithm, (b) the BPF algorithm, and (c) the MDFBP algorithm on a horizontal line passing through the ROI in the image space. For comparison, the corresponding true profile (dashed line) is also included. Again, one can observe that the BPF and MDFPB algorithms can reconstruct accurate images from a truncated data set. Furthermore, we also reconstructed noisy ROI images from the truncated data set containing noise by use of (a) the conventional FBP algorithm, (b) the BPF algorithm, and (c) the MDFBP algorithm to reconstruct noisy images, which are shown in Fig. 12. In the presence of data noise, both BPF and MDFBP algorithms can stably reconstruct ROI images from truncated noisy data. We have also performed a preliminary quantitative study by computing the root mean square error (RMSE) within the ROI between the true image and the images reconstructed by use of the algorithms discussed. For the noiseless case under study, the RMSE values for the conventional FBP algorithm, the BPF algorithm, and the MDFBP algorithm are 1.47×10^{-3}, 2.8×10^{-4}, and 2.9×10^{-4}, respectively; whereas for the noisy case under study, the RMSE values for the conventional FBP algorithm, the BPF algorithm, and the MDFBP algorithm are 1.51×10^{-3}, 5.0×10^{-4}, and 5.1×10^{-4}, respectively.

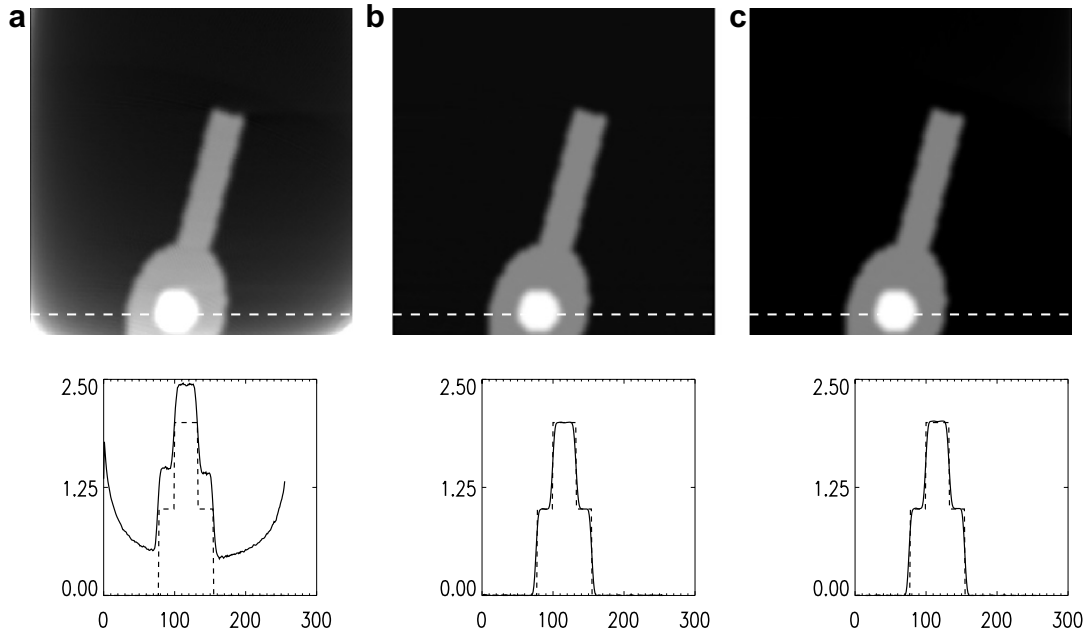

Fig. 11. Upper row: ROI images reconstructed from the truncated data set in Fig. 8b by use of (a) the conventional FBP algorithm, (b) the BPF algorithm, and (c) the MDFBP algorithm. Lower row: image profiles (solid curves) obtained by use of (a) the conventional FBP algorithm, (b) the BPF algorithm, and (c) the MDFBP algorithm on the horizontal lines passing the ROI in the upper row. We also display the true profile (dashed line) for comparison. The display window is [0.0, 2.0]. In (b) and (c) it can be observed that the solid lines virtually conicide with the dashed lines, indicating that the proposed algorithms can accurately reconstruct ROI images from truncated data. On the other hand, the result in (a) shows that the conventional FBP algorithm cannot accurately reconstruct ROI images from truncated data.

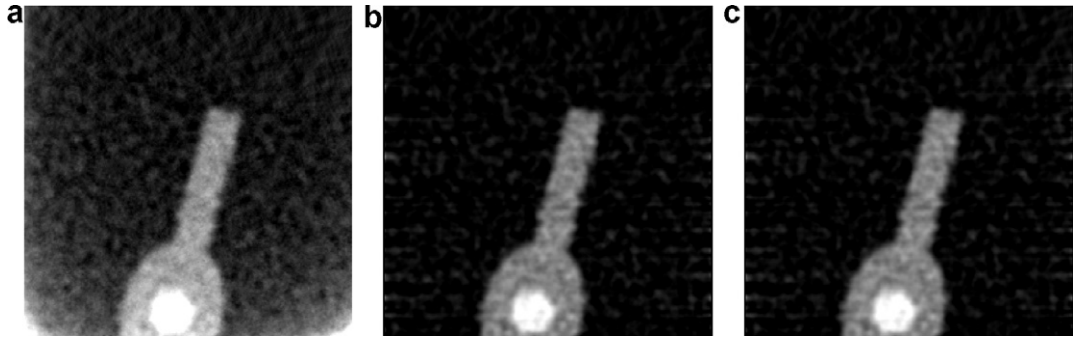

Fig. 12. ROI-images reconstructed from the truncated data set containing noise by use of (a) the conventional FBP algorithm, (b) the BPF algorithm, and (c) the MDFBP algorithm. The display window is [0.0, 2.0].

5.3. Spectral-Spatial images and truncation data

When both spatial and spectral dimensions are considered in 2D CW EPRI, the object function $f(x,B)$ is a 2D function of spatial variable x and spectral variable B, as show in Fig. 13. The object function in our EPRI experiment can be written as

$$f(x,B)=\begin{cases} f_{in}(x,B)\otimes g(B) & x\in[100,900] \text{ and } B\in[256,728] \\ 0 & \text{otherwise} \end{cases}, \tag{16}$$

where the intrinsic electron-spin distribution $f_{in}(x,B)$ and the convolution kernel are given by

$$f_{in}(x,B)=\frac{1}{1+(B-B_0)^2/\Delta B^2(x)}, \tag{17}$$

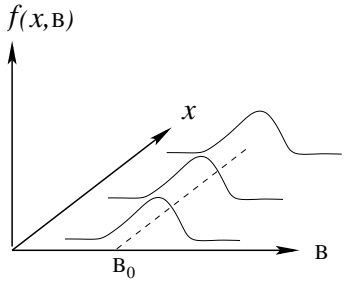

Fig. 13. Illustration of a 2D spectral-spatial object function $f(x,B)$, which is a function of a spatial variable x and a frequency variable B.

and $g(B)=\frac{1}{\sqrt{2\pi}\sigma}\exp(-\frac{B^2}{2\sigma^2})$. As shown in Eq. (17), the intrinsic function $f_{in}(x,B)$ reaches its peak at B_0 and has a the full width half maximum (FWHM) $\Delta B(x)$. (In the study, we have assumed that B_0 is independent of x. How-

ever, it can readily be generalized to a study in which B_0 is spatially varying.). Throughout the study, B, B_0, and ΔB have a unit of mG (milligauss, equal to 0.1 microtesla), whereas x has a unit of mm.

In this study, using Eq. (16), we have generated two different spectral-spatial object functions, as shown in Figs. 14a and 15a, which are specified by

$$\Delta B(x) = 30 - 0.025x \qquad x \in [100, 900], \tag{18}$$

and

$$\Delta B(x) = \begin{cases} 30 - 0.057(x - 100) & x \in [100, 450] \\ 10.0 & x \in [450, 550] \\ 30 - 0.057(900 - x) & x \in [550, 900] \end{cases},$$

In both cases, parameters $B_0 = 500$ mG and $\sigma = 25$ mG were used. Furthermore, we consider image reconstructions within two ROIs, which are specified by $x \in [860,920]$ and $B \in [256,728]$ and by $x \in [480,544]$ and $B \in [256,728]$, respectively, as indicated by the rectangular regions enclosed by the solid white lines in 14a and 15a. The values of these parameters were selected by considering the conditions in typical EPRI experiments.

From the 2D spectral-spatial functions, we have generated non-truncated Radon transforms, which are displayed in Figs. 14b and 15b, respectively. We also show in 14c and 15c the reduced data necessary for reconstructing the ROI images. It can be observed that these data functions are truncated and that they are considerably less than the full data shown in Figs. 14b and 15b. In both studies, data were generated at 512 projections uniformly distributed over [0, π] each of which contains 256 samples.

5.4. Reconstruction of 2D spectral-spatial ROI images

We have used both the conventional FBP algorithm and the BPF algorithm to reconstruct the spectral-spatial images from the full data in Figs. 14b and 15b. In this case, the results, which are not shown here, from both algorithms are virtually identical, indicating both algorithms perform equally well when full scan data are considered. From the truncated data shown in Figs. 14c and 15c, we have also used the conventional FBP algorithm and the BPF algorithm to reconstruct ROI images. In Figs. 16a and 17a, we show the images reconstructed by use of the FBP algorithm (A) and the BPF algorithm (B) for the two ROIs indicated in Figs. 14a and 15a, respectively. For comparison, the corresponding true ROI images are also displayed in panel (C) in both Figs. 16a and 17a. In

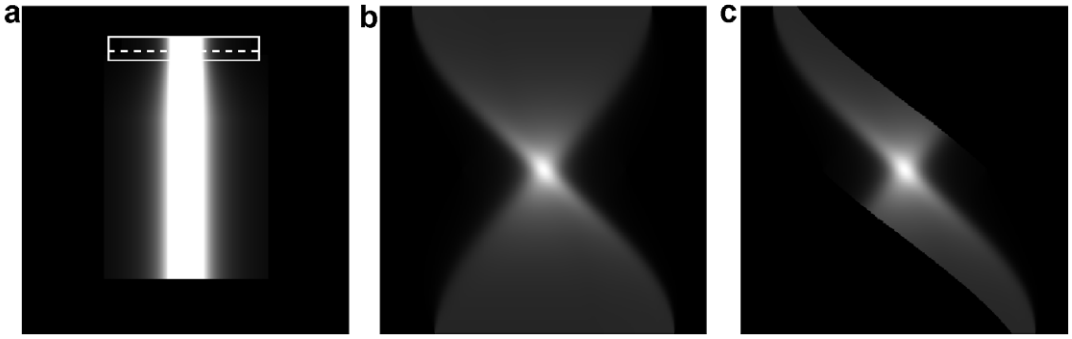

Fig. 14. (a) The spectral-spatial object function. An ROI is enclosed by the solid white lines. The vertical and horizontal axes indicate the x and B dimensions, respectively. The display window is [0.0, 0.01]. (b) The full Radon transform of the object function in (a). (c) The truncated Radon transform necessary for for image reconstruction within the indicated ROI. In both (b) and (c), the vertical and horizontal axes indicate the projection views and samples, respectively.

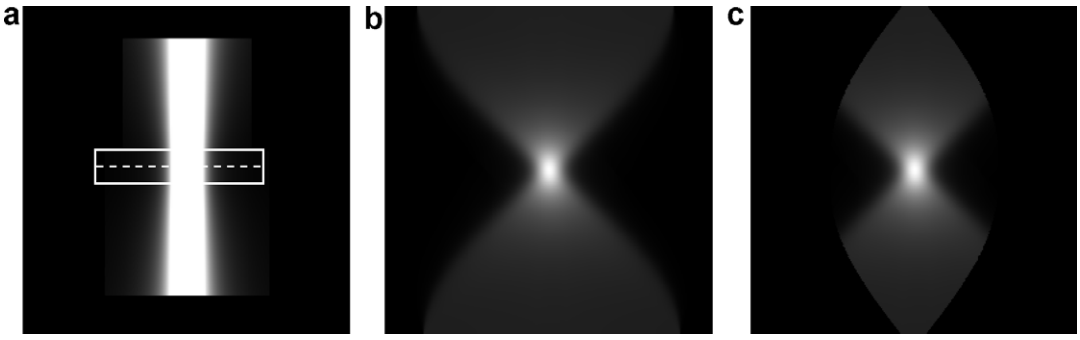

Fig. 15. (a) The spectral-spatial object function. An ROI is enclosed by the solid white lines. The vertical and horizontal axes indicate the x and B dimensions, respectively. The display window is [0.0, 0.01]. (b) The full Radon transform of the object function in (a). (c) The truncated Radon transform necessary for for image reconstruction within the indicated ROI. In both (b) and (c), the vertical and horizontal axes indicate the projection views and bins, respectively.

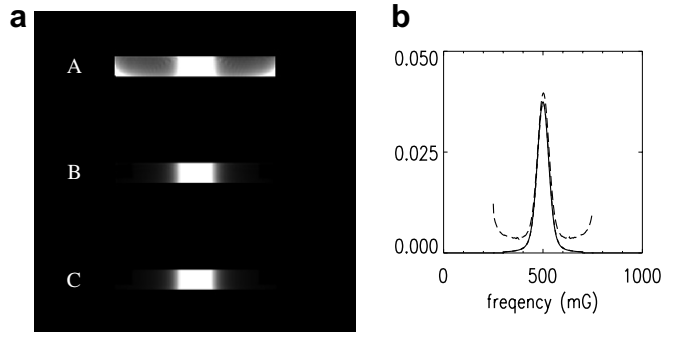

Fig. 16. (a) ROI images reconstructed by use of the conventional FBP algorithm (A) and the BPF algorithm (B) from the truncated data in Fig. 14c. The true ROI image is also shown in (C). The display window is [0.0, 0.01]. (b) Image profiles obtained by use of the conventional FBP algorithm (dashed) and the BPF algorithm (dotted), respectively, along the white dashed line indicated in Fig. 14a. The true profile (solid) is also displayed for comparison. The profile obtained with the BPF algorithm virtually coincides with the true profile, whereas the profile obtained with the conventional FBP algorithm differs significantly from the true profile.

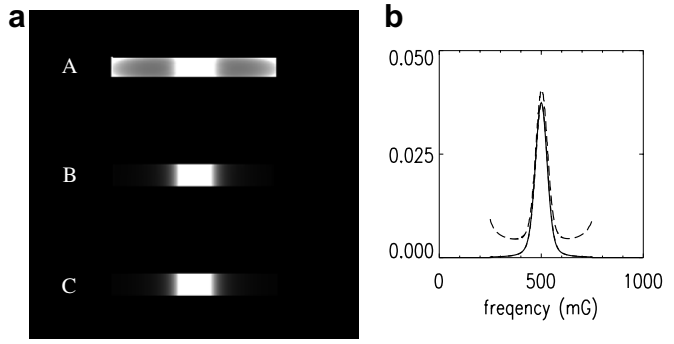

Fig. 17. (a) ROI images reconstructed by use of the conventional FBP algorithm (A) and the BPF algorithm (B) from the truncated data in Fig. 15c. The true ROI image is also shown in (C). The display window is [0.0, 0.01]. (b) Image profiles obtained by use of the conventional FBP algorithm (dashed) and the BPF algorithm (dotted), respectively, along the white dashed line indicated in Fig. 15a. The true profile (solid) is also displayed for comparison. The profile obtained with the BPF algorithm virtually coincides with the true profile, whereas the profile obtained with the conventional FBPalgorithm differs significantly from the true profile.

an attempt to demonstrate quantitatively the reconstruction accuracy, we also plot in Figs. 16b and 17b the ROI-image profiles on the dashed lines indicated in Figs. 14a and 15a. Specifically, the dashed and dotted curves represent the ROI-image profiles obtained with the the conventional FBP algorithm and the BPF algorithm. For comparison, we also plot the corresponding true profiles as the solid curves. It can be observed that the BPF profiles virtually coincide with the corresponding true profiles, indicating that the BPF algorithm can accurately reconstruct spatial-spectral ROI images from truncated data. In contrast, the results in Figs. 16 and 17 demonstrate that the conventional FBP algorithm cannot yield accurate reconstruction from truncated data. We have also computed the RMSEs within the reconstructed ROI regions. For the two ROIs indicated in Figs. 14a and 15a, the RMSEs yielded by the BPF algorithm are 6.1×10^{-6} and 6.2×10^{-6}, whereas the RMSEs produced by the conventional FBP algorithm are 1.1×10^{-4} and 1.2×10^{-4}, respectively.

6. Conclusions

In the work reported here, we have described the BPF and MDFBP algorithms and discussed their applications to reconstructing images in CW EPRI. A significant advantage of the BPF and MDFBP algorithms over the conventional FBP algorithm is that the former are capable of accurate ROI-image reconstruction from truncated Radon transforms of even dimension, whereas the latter cannot. We have also performed numerical studies to validate and demonstrate the performance of the BPF and MDFBP algorithms in ROI-image reconstruction. Quantitative results in these studies confirm that accurate ROI images can be obtained from truncated Radon transforms by use of the BPF and MDFBP algorithms.

An increased number of chords may improve reconstruction accuracy. This is not, however, unique to chord-based reconstruction. For example, in conventional approaches, improved reconstruction accuracy may also be obtained by use of an increased number of pixels. It is important, however, to recognize that increasing the number of chords (or pixels) beyond certain points will not lead to additional, appreciable improvement on image accuracy, which is ultimately determined by discrete data. In our numerical study, we used a number of chords (or pixels) beyond which no additional appreciable improvement can be derived. We have performed additional studies in which more chords than what was presented in the manuscript were used. The results of these additional studies showed that they lead to no appreciable improvement on image accuracy.

For a given ROI, based upon the BPF algorithm or the MDFBP algorithm, one can readily determine the amount of data sufficient for accurate ROI-image reconstruction. As demonstrated in Fig. 8b, we have determined data sufficient for accurate image reconstruction within the ROI shown in Fig. 11. Clearly, the Radon transform in Fig. 8b is severely truncated. This directly translates into reduced acquisition time. The physiologic importance of such a reduction cannot be overstated. As indicated by among others such as Braun et al [24], physiologic variations occur at a variety of time scales. It should also be mentioned that, due to the sensitivity of spectral fitting to spectral support, the projections are not likely to be truncated in the spectral dimension. However, as indicated here, significant truncation can be performed in the spatial dimension. The computational load of the BPF and MDFBP algorithms are comparable to that of the conventional FBP algorithm. The BPF algorithms have important practical implications for CW EPRI because their capability of accurate ROI-image reconstruction can be exploited for reducing imaging time by acquiring less data than that

for a complete scan. The benefits of substantially reducing imaging time include the reduction of motion and contrast-agent wash-out artifacts. It also allows the possible performance of temporally longitudinal studies by using the same animal repeatedly.

Acknowledgments

This work was supported in part by National Institutes of Health Grants EB000225, EB002765, P41-EB002034, EB02765, and CA98575 and DOD Grant PC061210. Its contents are solely the responsibility of the authors and do not necessarily represent the official views of the National Institutes of Health nor the Department of Defense.

References

[1] G.R. Eaton, S.S. Eaton, K. Ohno, EPR Imaging and *In Vivo* EPR, CRC Press, Inc., Boca Raton, 1991.
[2] H.J. Halpern, D.P. Spencer, J. van Polen, M.K. Bowman, R.J. Massoth, A.C. Nelson, E.M. Dowey, B.A. Teicher, An imaging radiofrequency electron spin resonance spectrometer with high resolution and sensitivity for in vivo measurements, Rev. Sci. Instrum. 60 (1989) 1080–1090.
[3] P. Kuppusamy, M. Chzhan, K. Vij, M. Shteynbuk, D.J. Lefer, E. Giannella, J.L. Zweier, Three-dimensional spectral-spatial EPR imaging of free radicals in the heart: a technique for imaging tissue metabolism and oxygenation, Proc. Natl. Acad. Sci. 91 (1994) 3388–3392.
[4] M. Elas, K.-H. Ahn, A. Parasca, E.D. Barth, D. Lee, C. Haney, H.J. Halpern, Electron paramagnetic resonance oxygen images correlate spatially and quantitatively with OxyliteTM oxygen measurements, Clin. Ca. Res. 12 (2006) 4209–4217.
[5] M. Elas, B.B. Williams, A. Parasca, C. Mailer, C.A. Pelizzari, M.A. Lewis, J. Rivers, G.S. Karczmar, E.D. Barth, H.J. Halpern, Quantitative tumor oxymetric images from 4D electron paramagnetic resonance imaging (EPRI): methodology and comparison with blood oxygen level-depednet (BOLD) MRI, Magn. Reson. Med. 49 (2003) 682–691.
[6] H.J. Halpern, M.K. Bowman, Low frequency EPR spectrometers: MHz range, in: G.R. Eaton, S.S. Eaton, K. Ohno (Eds.), EPR Imaging and *In Vivo* EPR, CRC Press, Boca Raton, FL, 1991.
[7] J.A. Brivati, A.D. Stevens, M.C.R. Symons, A radiofrequency ESR spectrometer for *in* vivo imaging, J. Magn. Reson. 92 (1991) 480–489.
[8] M. Alecci, S.D. Penna, A. Sotgiu, L. Testa, I. Vannucci, Electron paramagnetic resonance spectrometer for three-dimensional *in vivo* imaging at very low frequency, Rev. Sci. Instrum. 63 (1992) 42–63.
[9] H.J. Halpern, C. Yu, M. Peric, E. Barth, D.J. Grdina, B.A. Teicher, Oxymetry deep in tissues with low-frequency electron paramagnetic resonance, Proc. Nat. Acad. Sci. 91 (1994) 13047–13051.
[10] X. Pan, B. Williams, and H. Halpern. 3D and 4D EPRI: A Theoretical Investigation. In Y. Bizais, editor, Proc. of the Vllth Inter. Conf. on Fully 3D Reconstruction in Radiology and Nuclear Medicine, pages Fr-AMl-1, 2003.
[11] B. Williams, X. Pan, H. Halpern, EPR imaging: the relationship between CW spectra acquired from an extended sample subjected to fixed stepped gradients and the Radon transform of the resonance density, J. Magn. Reson. 174 (2005) 88–96.
[12] B.H. Robinson, C. Mailer, A.W. Reese, Linewidth analysis of spin labels in liquids. I. Theory and data analysis, J. Magn. Reson. 138 (1999) 199–209.
[13] B.H. Robinson, C. Mailer, A.W. Reese, Linewidth analysis of spin labels in liquids. II. Experimental, J. Magn. Reson. 138 (1999) 210–219.
[14] F. Noo, R. Clackdoyle, J. Pack, A two-step Hilbert transform method for 2D image reconstruction, Phys. Med. Biol. 49 (2004) 3903–3923.
[15] X. Pan, A unified reconstruction theory for diffraction tomography with considerations of noise control, J. Opt. Soc. Am. 15 (1998) 2312–2326.
[16] M.M. Maltempo, S.S. Eaton, G.R. Eaton, Spectral-spatial two-dimensional EPR imaging, J. Magn. Reson. 72 (1987) 449–455.
[17] F. Natterer, The Mathematics of Computerized Tomography, J. Wiley & Sons, New York, 1986.
[18] S.R. Deans, The Radon Transform and Some of its Applications, Krieger Publishing Company, Malabar, Florida, 1993.
[19] Y. Zou, X. Pan, Exact image reconstruction on Pi-line from minimum data in helical cone-beam CT, Phys. Med. Biol. 49 (2004) 941–959.
[20] J.D. Pack, F. Noo, R. Clackdoyle, Cone-beam reconstruction using the backpro-jection of locally filtered projections, IEEE Trans. Med. Imaging 24 (2005) 2317–2336.
[21] Y. Zou, X. Pan, E.Y. Sidky, Theory and algorithms for image reconstruction on chords and within regions of interest, J. Opt. Soc. Am. 22 (2005) 2372–2384.
[22] X. Pan, Y. Zou, Image reconstruction in regions of interest from truncated Radon transform of even dimensions, Inv. Prob. 21 (2005) 1169–1177.
[23] E.Y. Sidky, Y. Zou, X. Pan, Minimum data image reconstruction algorithms with shift-invariant filtering for helical, cone-beam CT, Phys. Med. Biol. 50 (2005) 1643–1657.
[24] R.D. Braun, J.L. Lanze, M.W. Dewhirst, Fourier analysis of fluctuations of oxgyen tension and blood flow in R3230Ac tumors and muscle in rats, Am. J. Physiol. 277 (1999) 551–568.